# Deciphering Water Oxidation Catalysts: The Dominant Role of Surface Chemistry over Reconstruction Degree in Activity Promotion

Li An[1], Jianyi Li[1], Yuanmiao Sun[2,3], Jiamin Zhu[1], Justin Zhu Yeow Seow[2], Hong Zhang[4], Nan Zhang[1], Pinxian Xi[1,5 ✉], Zhichuan J. Xu[2 ✉], Chun-Hua Yan[1,6]

HIGHLIGHTS

- Demonstrate that the key factor to determine the activity of reconstructed surfaces is the surface chemistry, instead of reconstruction degree using the popular perovskite $LaNi_{1-x}Fe_xO_3$ oxides as model materials.

- Fe content can influence both the surface reconstruction degree, the activation degree, and the activity of reconstructed surfaces.

- The oxygen evolution reaction activity of reconstructed catalysts is primarily governed by the chemistry of the reconstructed surface species.

ABSTRACT Water splitting hinges crucially on the availability of electrocatalysts for the oxygen evolution reaction. The surface reconstruction has been widely observed in perovskite catalysts, and the reconstruction degree has been often correlated with the activity enhancement. Here, a systematic study on the roles of Fe substitution in activation of perovskite $LaNiO_3$ is reported. The substituting Fe content influences both current change tendency and surface reconstruction degree. $LaNi_{0.9}Fe_{0.1}O_3$ is found exhibiting a volcano-peak intrinsic activity in both pristine and reconstructed among all substituted perovskites in the $LaNi_{1-x}Fe_xO_3$ ($x=0.00, 0.10, 0.25, 0.50, 0.75, 1.00$) series. The reconstructed $LaNi_{0.9}Fe_{0.1}O_3$ shows a higher

intrinsic activity than most reported NiFe-based catalysts. Besides, density functional theory calculations reveal that Fe substitution can lower the O $2p$ level, which thus stabilize lattice oxygen in $LaNi_{0.9}Fe_{0.1}O_3$ and ensure its long-term stability. Furthermore, it is vital interesting that activity of the reconstructed catalysts relied more on the surface chemistry rather than the reconstruction degree. The effect of Fe on the degree of surface reconstruction of the perovskite is decoupled from that on its activity enhancement after surface reconstruction. This finding showcases the importance to customize the surface chemistry of reconstructed catalysts for water oxidation.
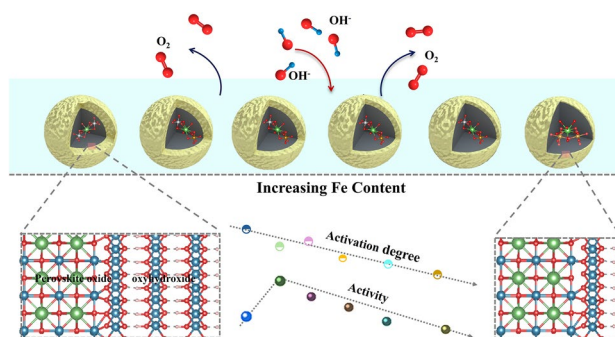
KEYWORDS Oxygen evolution reaction; Perovskite oxides; Doping; Activation and reconstruction

Li An, Jianyi Li, Yuanmiao Sun, and Jiamin Zhu have contributed equally to this work.

✉ Pinxian Xi, xipx@lzu.edu.cn; Zhichuan J. Xu, xuzc@ntu.edu.sg

1 State Key Laboratory of Applied Organic Chemistry, Key Laboratory of Nonferrous Metal Chemistry and Resources Utilization of Gansu Province, Frontiers Science Center for Rare Isotopes, College of Chemistry and Chemical Engineering, Lanzhou University, Lanzhou 730000, People's Republic of China

2 School of Materials Science and Engineering, Nanyang Technological University, Singapore 639798, Singapore

3 Faculty of Materials Science and Energy Engineering, Institute of Technology for Carbon Neutrality, Shenzhen Institute of Advanced Technology, Chinese Academy of Sciences, Shenzhen 518055, People's Republic of China

4 Key Laboratory of Electromagnetic Materials and Devices, National Center for International Research On Photoelectric and Energy Materials, School of Materials and Energy, Electron Microscopy Center, Yunnan University, Kunming 650091, People's Republic of China

5 State Key Laboratory of Baiyunobo Rare Earth Resource Researches and Comprehensive Utilization, Baotou Research Institute of Rare Earths, Baotou 014030, People's Republic of China

6 Beijing National Laboratory for Molecular Sciences, State Key Laboratory of Rare Earth Materials Chemistry and Applications, PKU-HKU Joint Laboratory in Rare Earth Materials and Bioinorganic Chemistry, Peking University, Beijing 100871, People's Republic of China

1 Introduction

The increasing demands of global energy consumption call for a sustainable and environmentally friendly energy supply [1]. Hydrogen offers one of the most promising solutions because of its zero-carbon attribute [2]. Electrochemical water splitting is a clean and direct approach to producing green hydrogen, provided that the electrolyzer can be powered by electricity obtained from renewable sources [3, 4]. However, the efficiency of water splitting is technically hindered by the sluggish oxygen evolution reaction (OER) at the anode, which necessitates the design of efficient OER electrocatalysts [5, 6].

Transition metal perovskite oxides have been demonstrated recently as a class of materials capable to efficiently catalyze OER in alkaline condition [7]. The ABO_3 crystal frame of perovskites enables the A and B sites to be resided by alkali/alkaline-earth/rare earth metals and first-row transition metals, respectively. Within the structure, the A- and/or B-site cations can be substituted by a foreign cation having different radius or oxidation state [8]. Therefore, the composition and cation oxidation state of perovskites are highly manipulable, which offers a feasible and convenient way to correlate the physicochemical properties with the catalytic performance of perovskite-type oxides, $LaNiO_3$ is a well-known conducting material ($\rho = 9 \times 10^{-3}$ Ω cm) at room temperature because of the stable low-spin (LS) $t_{2g}^6 e_g^1$ configuration of $Ni^{3+}(d^7)$ [9–11]. It has been found that OER catalyzed by $LaNiO_3$, especially by the compressively strained $LaNiO_3$, prefers to proceed via lattice oxygen mechanism (LOM) rather than adsorbate evolution mechanism (AEM) [12, 13]. The activation of lattice oxygen in LOM implies that the structure of perovskite $LaNiO_3$ may easily undergo dynamic in-situ structural reconstruction under OER conditions. More recently, it has been reported that the structure of nickel-based transition metal oxides (TMOs) can easily transform into oxyhydroxides after long-term electrochemical cycling, enabling the in-situ generated NiOOH to function as the real active species for OER [14].

However, the OER activity of pure NiOOH is found to be relatively poor. It has been intensively observed that the presence of Fe in nickel-based oxyhydroxides, either directly incorporated in the pre-catalyst or accidentally deposited from electrolyte solution, can effectively improve the catalytic activity of the electrode [15–19]. Although it remains debatable whether nickel or iron cations serve as the active centers, the optimal metallic fraction of iron in nickel–iron oxyhydroxide is found to be less than 30% (nickel higher than 70%) [20]. Meanwhile, the degree to which the original perovskite phase can reconstruct during OER also contribute to the measured activity by influencing the number of available active sites. The reconstruction behavior is highly sensitive to the bulk chemistry of perovskite. It is critical to identify the optimal nickel–iron ratio in perovskite pre-catalyst to optimize its degree of reconstruction and subsequent oxyhydroxide OER activity [21].

In this work, using perovskite $LaNi_{1-x}Fe_xO_3$ ($x = 0.00, 0.10, 0.25, 0.50, 0.75,$ and 1.00, which was simplified as $LaNi_{1-x}Fe_xO_3$ below) as model catalysts, we investigate the role of iron cations during surface reconstruction and reveal the optimal nickel–iron ratio in the perovskite pre-catalyst. Our results show that the activity of the reconstructed $LaNi_{0.9}Fe_{0.1}O_3$ outperforms other perovskites, and its intrinsic activity is even higher than some benchmark NiFe-based catalysts. The low level of Fe substitution in $LaNiO_3$ obviously accelerates the reconstruction rate and enables enhanced activity in both its pristine and reconstructed state. However, since reconstructed $LaNiO_3$ with the maximum reconstruction degree exhibits lower OER activity than reconstructed $LaNi_{0.9}Fe_{0.1}O_3$, the effect of Fe doping on the degree of surface reconstruction of the perovskite is effectively decoupled from that on its OER activity enhancement after electrochemical treatment. Unveiled by density functional theory (DFT) calculations, $LaNi_{0.9}Fe_{0.1}O_3/Ni_{0.9}Fe_{0.1}OOH$ with balanced reconstruction degree and reconstruction rate was demonstrated as the most stable interface structure. Besides, Fe substitution lowers the O $2p$ level and thus stabilizes the lattice oxygen in $LaNi_{0.9}Fe_{0.1}O_3$. As a result, Fe incorporation creates more stable surface chemistry to provide enhanced structural stability compared with pure $LaNiO_3$. The surface amorphous layer composed of $Ni_{0.9}Fe_{0.1}OOH$ with atomic Fe incorporated Ni sites as active sites showing obvious electronic activity can further ensure enhanced activity and long-term stability under OER conditions.

2 Experimental Section

2.1 Materials

Lanthanum (III) nitrate hexahydrate ($La(NO_3)_3 \cdot 6H_2O$, 99.9%), nickel (II) acetate hexahydrate ($Ni(OAc)_2 \cdot 6H_2O$,

99.0%), iron (III) nitrate nonahydrate ($Fe(NO_3)_3 \cdot 9H_2O$, 98.5%), urea ($CO(NH_2)_2$, 99.0%), citric acid monohydrates ($C_6H_8O_7 \cdot H_2O$, 99.5%), potassium hydroxide (KOH, 99.9%), and Nafion® (5 wt%) were purchased from Aladdin. The deionized (DI) water was obtained from a Millipore Autopure system (18.2 MΩ, Millipore Ltd., USA). Oxygen gas was of 5 N quality (99.999%, Airgas). All the other materials for electrochemical measurements were of analytical grade and were used without further purification.

2.2 Preparation of $LaNi_{1-x}Fe_xO_3$

$LaNi_{1-x}Fe_xO_3$ powders were synthesized by a sol–gel method. The $LaNiO_3$ precursors were produced by dissolving 3.75 mmol $La(NO_3)_3 \cdot 6H_2O$, 3.75 mmol $Ni(OAc)_2 \cdot 6H_2O$, 15 mmol urea, 15 mmol citric acids in 30 mL of deionized (DI) water and 3 mL of nitric acid. As for $LaNi_{1-x}Fe_xO_3$, $Fe(NO_3)_3 \cdot 9H_2O$ and $Ni(OAc)_2 \cdot 6H_2O$ were added stoichiometrically for Fe to replace Ni. $LaFeO_3$ precursor was prepared by using 3.75 mmol $Fe(NO_3)_3 \cdot 9H_2O$ instead of $Ni(OAc)_2 \cdot 6H_2O$. Increasing the heating temperature to 150 °C with a stable magnetic stirring until the above precursor solutions become a gel state. Then, the gel was dried at 170 °C for 12 h to remove the remaining water and calcined at 600 °C in the O_2 atmosphere for 6 h.

2.3 Electrochemical Measurements

The as-synthesized $LaNi_{1-x}Fe_xO_3$ perovskite oxide (16 mg) was mixed with acetylene black (6.4 mg). The mixture was then dispersed in a mixed solution of water (6.4 mL), isopropanol (1.6 mL), and Nafion solution (100 μL) to prepare the homogeneous ink of the catalyst. The obtained catalyst ink was drop-casted on glassy carbon electrode (GC, with diameter of 5 mm) with a geometric area of 0.196 cm^2. The final mass loading of catalyst is 255 μg_{ox} cm^{-2}_{disk}.

All electrochemical measurements were performed at room temperature on a Biologic SP-150 workstation (Bio-Logic Science Instruments) using a conventional three-electrode setup. For OER in media (1.0 M KOH), a Pt plate and mercury-mercury oxide electrode (Hg/HgO) electrode (filled with 1.0 M KOH solution) were used as

counter and reference electrodes, respectively. The reference electrode was calibrated against reversible hydrogen electrode (RHE) in H_2-saturated electrolyte with Pt plates as both the working and counter electrodes, which should be consistent with the Eq. (1):

$$E(\text{vs. RHE}) = E(\text{vs. Hg/HgO}) + 0.098 + 0.059 \times \text{pH} \quad (1)$$

Before the electrochemical measurement, the KOH electrolyte was degassed by bubbling oxygen for at least 30 min to obtain the oxygen gas saturated condition. All electrochemical experiments were conducted at 20 ± 0.2 °C. Cyclic voltammetry (CV) was set at the alternating scan rates of 10 mV s^{-1} and 100 mV s^{-1}. Here, we used the data of the 2nd and 5000th cycles (without further obvious current increase in the subsequent cycles) to represent pre-catalysts and reconstructed catalysts respectively for characterization and analysis. These cycles were collected at a scan rate of 10 mV s^{-1}. For the intermediate cycles, a scan rate of 100 mV s^{-1} was applied. Tafel slopes were obtained by averaging the positive-going and negative-going scans of CV curves obtained with the scan rate of 10 mV s^{-1}. These data were collected and corrected for the uncompensated (iR) contribution within the cell through Eq. (2):

$$E_{real} = E(\text{vs. RHE}) - iR \quad (2)$$

For the analysis of the correlations between reconstruction degree, activation degree and OER activity, reconstruction degree and activation degree have been defined as follow Eq. (3):

$$\text{Reconstruction degree} = t/1 \text{ nm} \quad (3)$$

where t represents the thickness of the newly formed reconstructed surface layer.

Activation degree $= \Delta j / j_{\text{as-synthesized}}$, where Δj represents the change in current density after activation relative to current density before activation ($j_{\text{reconstructed}} - j_{\text{as-synthesized}}$).

2.4 Computational Details

The Vienna Ab-initio Simulation Package (VASP) was carried out for the $LaNi_{1-x}Fe_xO_3$ system calculations [55]. The Perdew–Burke–Ernzerhof (PBE) functional, within the generalized gradient approximation (GGA) approach, was used to describe the exchange and correlation effects. For

all the geometry optimizations, the cutoff energy was set to 450 eV. The force and energy convergence tolerance were set to be 0.05 eV $\mathring{A}^{-1}$ and 10^{-5} eV, respectively. The models of $LaNi_{1-x}Fe_xO_3$ ($x = 0.00$, 0.10, 0.25, 0.50, 0.75, and 1.00) supercells were constructed by replacing Fe atoms with Ni atoms in a $LaFeO_3$ structure. The Monkhorst–Pack k-point mesh was set to be $6 \times 6 \times 2$ and $6 \times 6 \times 4$ for performing calculations on $LaNi_{1-x}Fe_xO_3$ ($x = 0.00$, 0.10, 0.25, 0.50, 0.75, 1.00). The Hubbard U corrections were adopted using the model proposed by Dudarev and colleagues. The Uef (Uef = Coulomb (U)–exchange (J)) values of Ni and Fe were set to be 6.4 and 4 eV, respectively. The pure heterostructure is composed of three amorphous NiOOH layers and two crystalline $LaNiO_3$ layers. The Fe doped only has two NiFeOOH layers. The molecular dynamics simulation was adopted to calculate the amorphous structure for 1.5 ps with a time step of 1 fs. The GGA-PBE functional is selected for the exchange and correlation potential [56]. Weak van der Waals interaction is considered by the DFT-D_3 functional [57]. The cut off energy for the plane-wave is 400 eV. The Gamma point in the Brillouin-zone is chosen for integration. Total energies of the systems converge to 10^{-5} eV in the iteration solution of Kohn–Sham equation. The force on each atom reduces to 0.05 eV $\mathring{A}^{-1}$ after geometry optimization. The amorphous structure is built by ab-initio molecular dynamics simulation using Nosé-Hoover thermostat for 1.7 ps with a time step of 1 fs [58]. The crystalline structure is melted at 3500 K for 0.6 ps, which was then quenched to the room temperature (300 K) for 1.1 ps.

3 Results and Discussion

3.1 Crystal and Electronic Structure Analysis

Perovskite $LaNi_{1-x}Fe_xO_3$ with different Fe contents was prepared using a sol–gel method [22]. Demonstrated by the inductively coupled plasma optical emission spectroscopy (ICP-OES), the actual amounts of Fe in the prepared system are quite close to that in the nominal stoichiometric composition (Table S1). The crystal structures of the $LaNi_{1-x}Fe_xO_3$ oxides were characterized by powder X-ray diffraction (XRD). As shown in Figs.1a and S1, no diffraction peaks of La_2O_3 and NiO can be found, demonstrating the formation of pure $LaNi_{1-x}Fe_xO_3$ oxide series without impurity. $LaNi_{0.5}Fe_{0.5}O_3$ exhibits a mixture of both the rhombohedral

and orthorhombic structures. Furthermore, with more Ni being replaced by Fe ($0.10 < x < 1.00$), an obvious diffraction peak shift toward a smaller angle is observed (Fig.S1). Such peak shift is ascribed to lattice expansion induced by the difference in ionic radii between Ni and Fe cations, which indicates the successful substitution of Ni by Fe [23, 24]. Field-emission scanning electron microscope (FE-SEM) images (Fig. S2) illustrate that all the as-synthesized $LaNi_{1-x}Fe_xO_3$ adopt similar morphology of irregular shapes. The transmission electron microscopy (TEM) image (Fig. S3) and the corresponding energy-dispersive spectrum (EDS) elemental mappings confirm the successful synthesis of $LaNi_{0.9}Fe_{0.1}O_3$ and La, Ni, Fe, and O are uniformly distributed in the entire architecture (Fig. S4). The atomic-resolution high-angle annular dark-field aberration-corrected scanning transmission electron microscopy (HAADF-STEM) image and corresponding EDS atomic elemental mappings were then carried out to disclose the position of the doped Fe in the $LaNiO_3$ host. As shown in Figs. 1b and S5, all the atoms are uniformly arranged and the doped Fe atoms display the same arrangement as Ni atoms, revealing the similar site geometrical occupation of Fe and Ni. Collectively, we can conclude that Fe doping into pure $LaNiO_3$ perovskite has resulted in only substitution of Ni ions [25]. This phenomenon can be rationalized by the electronic interaction between the host Ni and the dopant Fe, which thus modulates the local atomic coordination environment of NiO_6 motifs at B sites in perovskite structures [26].

It is observed that the majority valence states of nickel and iron cations are +3 in pure $LaNiO_3$ and $LaFeO_3$ conducted by X-ray photoelectron spectroscopy (XPS). However, small amounts of Ni^{2+} and Fe^{2+} are detected (Fig. S6), indicating the existence of oxygen vacancies on the surface [23, 27, 28]. With increasing Fe content in $LaNi_{1-x}Fe_xO_3$ ($x = 0.00$, 0.10, 0.25, 0.50, 0.75), Ni^{2+}/Ni^{3+} ratio increases (Fig. S7), demonstrating that introducing Fe into the $LaNi_{1-x}Fe_xO_3$ system reduces the oxidation state of Ni [29, 30]. The subtle changes of local bonding environments and coordination structures were investigated by X-ray absorption spectroscopy (XAS) [31]. The absorption edge energies were defined by the half-height approach [32, 33]. From Fig. 1c and d, absorption edge energies of both Ni and Fe decrease with Fe doping, further demonstrating the reduced oxidation states of metals and the interaction between host Ni and dopant Fe. The coordination environment and symmetry of metal centers can also be analyzed from the pre-edge feature of the metal K-edge
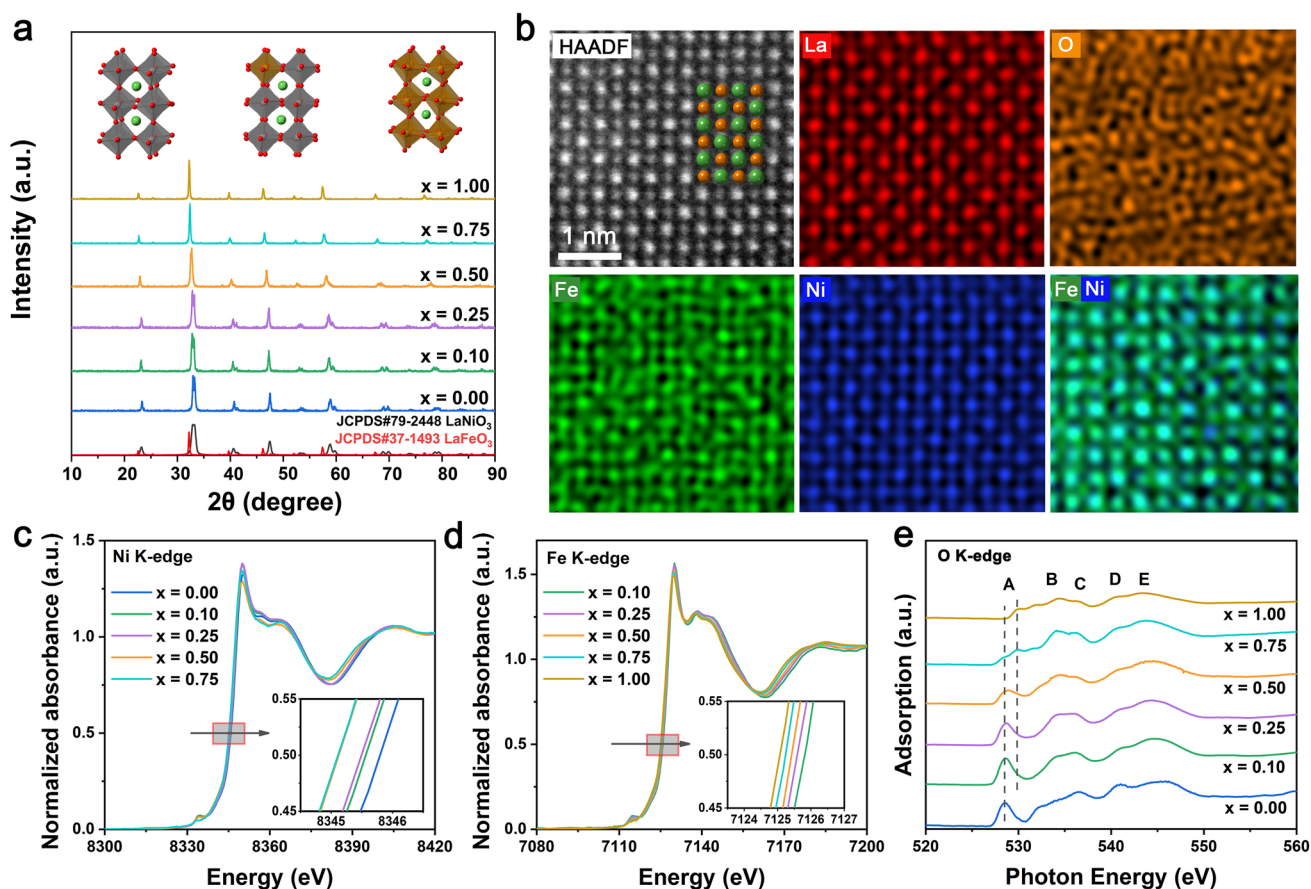
Fig. 1 **a** XRD patterns of $LaNi_{1-x}Fe_xO_3$ in comparison with the standard XRD patterns of $LaNiO_3$ (JCPDS 79-2448) and $LaFeO_3$ (JCPDS 37-1493). **b** Atomic-resolution HAADF-STEM image and corresponding EDS atomic elemental mapping images of $LaNi_{0.9}Fe_{0.1}O_3$. Inset shows the crystal structure scheme of $LaNi_{0.9}Fe_{0.1}O_3$ proposed based on the HAADF-STEM image, where yellow spheres represent La cations and red spheres represent Ni/Fe cations. **c** Normalized Ni K-edge XANES spectra for $LaNi_{1-x}Fe_xO_3$ ($x=0.00$, 0.10, 0.25, 0.50, 0.75). **d** Normalized Fe K-edge XANES spectra for $LaNi_{1-x}Fe_xO_3$ ($x=0.10$, 0.25, 0.50, 0.75, 1.00). Insets provide the magnified images of Ni K-edge XANES spectra and Fe K-edge XANES spectra. **e** O K-edge XAS spectra of $LaNi_{1-x}Fe_xO_3$

peak (Fig. S8, Note S1). Compared with pure $LaFeO_3$, the more pronounced pre-edge peak ($1s \rightarrow 3d$ state transition) of $LaNi_{1-x}Fe_xO_3$ ($x=0.10$, 0.25, 0.50, 0.75) suggests more distorted lattice arrangement [26, 34]. The lattice distortion may act as the structural origin for the dynamic structural evolution of $LaNi_{1-x}Fe_xO_3$ ($x=0.10$, 0.25, 0.50, 0.75) during electrochemical process. The Fourier transform (FT) of k_3-weighted extended X-ray absorption fine structure (EXAFS) characterization (Fig. S9) and the corresponding wavelet transformation (WT) analysis (Fig. S10) were further used to demonstrate the strong interaction between metals Ni and Fe. Besides, O K-edge XAS was also utilized to study the electronic structure of $LaNi_{1-x}Fe_xO_3$. The special peak A in the spectra can be attributed to the band hybridization between O $2p$ and M (Ni/Fe) $3d$. The obvious positive shift of peak A with increasing Fe

doping in $LaNiO_3$ further supports the inference of decreased metals valence after introducing Fe (Figs. 1e and S11) [27, 33, 35–37]. Electron energy loss spectroscopy (EELS) was performed on selected samples to further understand their electronic structures. For Ni L-edge and Fe L-edge, the negative shift of Ni L_3 from $x=0$ to $x=0.10$ and the reduced Fe L_3/L_2 ratio from $x=1.00$ to $x=0.10$ confirm the interaction between Ni and Fe (Fig. S12a and b). As observed by O K-edge of EELS, the disappearance of pre-peak located at around 531.5 eV indicates the decreased hybridization between O $2p$ and M $3d$ or an increase in oxygen vacancies (Fig. S12c). Owing to the changed oxidation states of Ni and Fe, the O $2p$-M $3d$ hybridization can be excluded, therefore the pre-peak disappearance in O K-edge EELS spectra is attributed to the formation of oxygen vacancies [35–38]. Besides,

EELS spectra of Ni L-edge and Fe L-edge were obtained from scans on $LaNi_{0.9}Fe_{0.1}O_3$ along the direction shown in Fig. S13. Compared with the stable peaks of Fe–L_3, the obvious positive shift of La-M_4/Ni-L_3 convoluted peak from Point 1 to Point 7 demonstrates that the oxidation state of outer Ni is much lower than that of inner Ni. This observation implies that the introduction of Fe causes the formation of oxygen vacancies in $LaNi_{0.9}Fe_{0.1}O_3$, which mainly exist at the surface of perovskite oxides (Fig. S14) [27]. Collectively, we can reasonably conclude that without damaging the main crystal structure in the bulk phase, surface oxygen vacancies and lattice distortions created by appropriate Fe substitution increase the flexibility of the perovskite structure, which can facilitate structural evolution under electrochemical treatment.

3.2 Electrochemical Characterizations and Activation Degree Analysis

The effect of Fe doping in perovskite oxides was further evaluated by their electrocatalytic performance. All potential data are converted to the reversible hydrogen electrode (RHE) scale for direct comparison. To avoid the possibility of Fe-impurity-induced activity enhancement, Fe-free electrolyte prepared from electronic grade KOH (99.999% purity) was used for the OER characterizations, detailed procedures of which are provided in Note S2. Figure 2a and b shows the cyclic voltammetry (CV) curves (normalized to the Brunauer–Emmett–Teller (BET) surface area, as shown in Table S2) of the as-synthesized and surface-reconstructed $LaNi_{1-x}Fe_xO_3$, respectively. We can see similar activity trends with $LaNi_{0.9}Fe_{0.1}O_3$ showing the best intrinsic activity. These trends are attributed to the introduction of Fe, which is consistent with recent reports that excess iron content would lead to Fe phase segregation and subsequent activity degradation [39, 40]. After surface reconstruction, the current density at 1.6 V of $LaNi_{0.9}Fe_{0.1}O_3$ increases and becomes comparable to that of the benchmark IrO_2 [41] in the OER regime (Fig. 2c). This indicates a surface reconstruction of the crystalline $LaNi_{0.9}Fe_{0.1}O_3$ that improved OER activity [42]. Moreover, by normalizing the activity with the number of redox-active sites, the intrinsic activity of reconstructed $LaNi_{0.9}Fe_{0.1}O_3$, expressed as turnover frequency (TOF, see Note S3) at an OER overpotential (η) of 300 mV, was compared with those of the state-of-the-art NiFe-based electrocatalysts in Fig. 2d. It is observed that

after surface activation, the intrinsic TOF of reconstructed $LaNi_{0.9}Fe_{0.1}O_3$ becomes superior to that of $LaNiO_3$-500 perovskite oxide [38], $Ni_{0.75}Fe_{0.25}OOH$ film [16], NiFeOOH film [43], and exfoliated NiFe layered double hydroxides (LDH) [44], manifesting the excellent OER activity of the reconstructed $LaNi_{0.9}Fe_{0.1}O_3$. This activation process can also be observed in the chronopotentiometry (CP) of pristine $LaNi_{0.9}Fe_{0.1}O_3$ at a current density of 10 mA cm^{-2} for about 20 h, which also shows excellent stability with a negligible potential increase over the next 80 h of the durability test (Fig. S15). This 100 h CP test also demonstrates the stability performance of $LaNi_{0.9}Fe_{0.1}O_3$. Furthermore, the almost unchanged morphology and structure observed from the XRD pattern and TEM images after long-term reaction suggest the robust structure stability of $LaNi_{0.9}Fe_{0.1}O_3$ (Fig. S16). Thus, $LaNi_{0.9}Fe_{0.1}O_3$ after activation has demonstrated as an ideal OER catalyst in terms of both activity and stability.

The reduction–oxidation behavior of $LaNi_{1-x}Fe_xO_3$ perovskite oxides can be studied through cyclic voltammograms of the pristine oxides and surface-reconstructed catalytic surfaces displayed in Figs. S17 and S18. Generally, for $x \le 0.50$, the redox peak areas and OER activities increase after the OER activation process, demonstrating the gradual activation of metal active sites underneath the pristine oxide surface [17, 45]. The subsequent surface reconstruction correlates with oxidation processes in the pre-OER regime [8, 46], which is sensitive to the Ni/Fe ratio of $LaNi_{1-x}Fe_xO_3$ oxides. The subsequent surface reconstruction correlates with oxidation processes in the pre-OER regime [8, 46], which is sensitive to the Ni/Fe ratio of $LaNi_{1-x}Fe_xO_3$ oxides. For detailed analysis, we take $LaNiO_3$ and $LaNi_{0.9}Fe_{0.1}O_3$ as our models for comparison. Compared with the as-synthesized $LaNiO_3$ that has only one clear pair of redox peaks, two reduction peaks and one oxidation peak can be observed for reconstructed $LaNiO_3$, in which the reduction peaks at ~1.34 and ~1.28 V are assigned to Ni(IV)/Ni(III) and Ni(III)/Ni(II), respectively (Fig. 2e). This suggests the presence of two reversible redox reactions; thus we believe that the anodic peak at ~1.39 V should be the result of the convolution of oxidation peaks attributed to Ni(II)/Ni(III) and Ni(III)/Ni(IV) transitions. For the as-synthesized $LaNi_{0.9}Fe_{0.1}O_3$, it possesses redox features similar to reconstructed $LaNiO_3$ (i.e., two resolved reduction peaks and one convoluted oxidation peak). However, the reduction peak of Ni(III)/Ni(II) disappears for reconstructed $LaNi_{0.9}Fe_{0.1}O_3$, demonstrating a much more stable Ni^{3+} state in $LaNi_{0.9}Fe_{0.1}O_3$
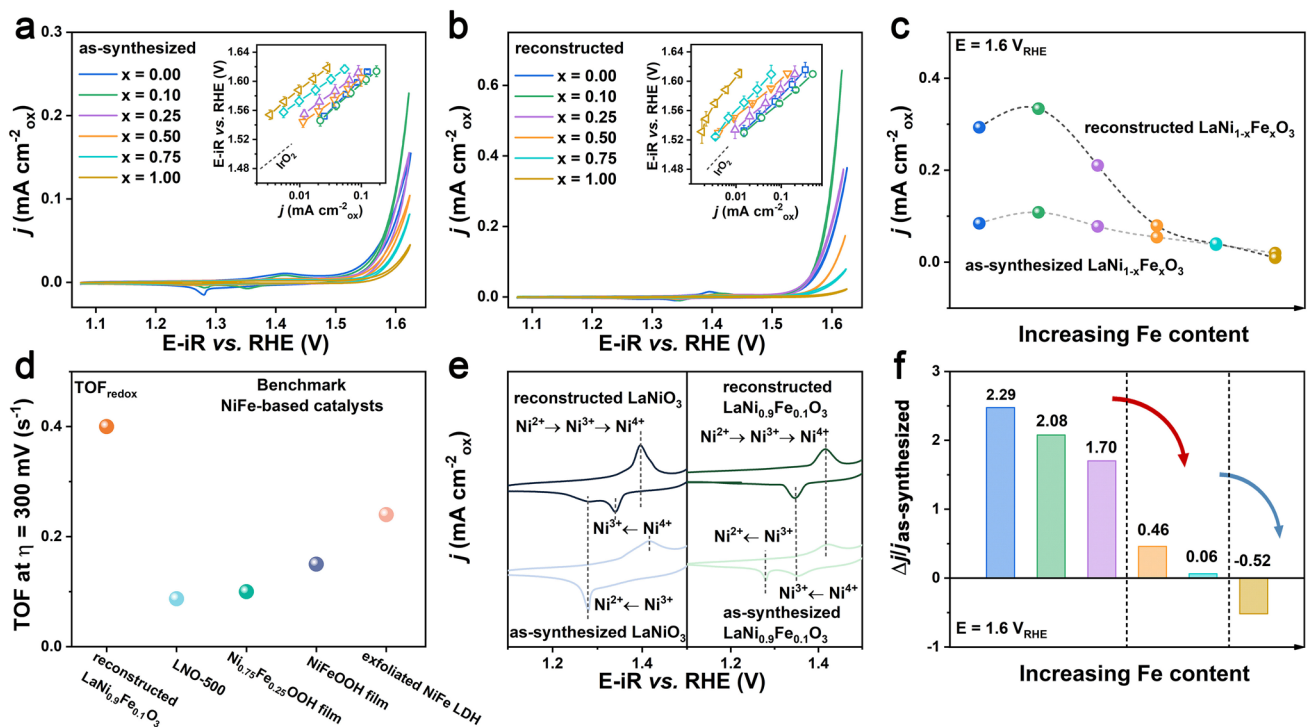
Fig. 2 **a** iR-corrected cyclic voltammograms (CVs) of as-synthesized $LaNi_{1-x}Fe_xO_3$. **b** iR-corrected CVs of reconstructed $LaNi_{1-x}Fe_xO_3$. Both sets of CVs were obtained during measurement in O_2-saturated 1.0 M KOH (99.999%) at a scan rate of 10 mV s^{-1}. Insets present the corresponding Tafel plots normalized by BET surface areas of (*A*) as-synthesized and (*B*) reconstructed $LaNi_{1-x}Fe_xO_3$ compared with IrO_2 [41]. Each error bar represents standard deviation of three independent measurements. **c** Surface area-normalized current densities (*j*) of the as-synthesized and reconstructed $LaNi_{1-x}Fe_xO_3$ at 1.6 V. **d** Turnover frequency (TOF) of the reconstructed $LaNi_{0.9}Fe_{0.1}O_3$ at an overpotential (η) of 300 mV. The number of active sites for TOF calculation is estimated by the coulombic charge under the M redox peak (TOF$_{redox}$) (see Note S3). **e** Evolution of redox behavior of representative $LaNiO_3$ (left) and $LaNi_{0.9}Fe_{0.1}O_3$ (right) perovskite oxides in 1.0 M KOH at 10 mV s^{-1} between 1.1 and 1.5 V. **f** Relative current change of $LaNi_{1-x}Fe_xO_3$, where the current densities were obtained at 1.6 V. All potential data are iR-corrected and Δj represents the change in current

than in $LaNiO_3$. Besides, the Ni oxidation peaks shift toward higher potentials upon Fe incorporation (Fig. S19), which can be used as an indicator of the presence of Fe in the main structure as demonstrated by many reports [25, 26]. This suggests a strong synergistic electronic interaction between Ni and Fe [47]. Meanwhile, the reduction peaks of Ni(IV)/Ni(III) also show a slight anodic shift upon the addition of Fe. These results imply that while it is more difficult to oxidize Ni^{3+} to Ni^{4+} in the presence of Fe, Ni^{4+} is more easily to be reduced to Ni^{3+} in reconstructed $LaNi_{0.9}Fe_{0.1}O_3$. Then, combined with the disappearance of Ni^{2+} after the activation process, we can conclude that incorporating Fe can facilitate Ni^{3+} to reach dynamic equilibrium for constructing a stable active layer in the presence of Ni^{3+} species. When looking into pure $LaFeO_3$, we notice that the areas for both the oxidation and reduction peaks (at ~ 1.38 and ~ 1.26 V, respectively) are much smaller than that of $LaNiO_3$ (Fig. S20a and

b), which can be overlooked in comparison with the CV curves of $LaNi_{0.9}Fe_{0.1}O_3$ [48]. Besides, the redox peaks of $LaFeO_3$ remain almost stable before and after reconstruction (Fig. S20c). Thus, we believe the reconstruction behavior is mainly contributed by Ni. Furthermore, we also estimated the charge involved in both the oxidation and reduction peaks of the $LaNi_{0.9}Fe_{0.1}O_3$ (Fig. S21; see Note S4) to study the redox of surface-active sites and their OER activity [18, 49]. The increased redox charge after activation (Table S3) suggests the enhanced oxidability/reducibility and intrinsic activity for reconstructed $LaNi_{0.9}Fe_{0.1}O_3$ oxide. We then attribute the related OER activity enhancement after surface reconstruction to the increment in the number of active sites [1], owing to the newly reconstructed surface.

By comparing average current densities (averaging the positive-going and negative-going scans), $LaNi_{0.5}Fe_{0.5}O_3$ and $LaNi_{0.25}Fe_{0.75}O_3$ show only slight positive current change. For

pure $LaFeO_3$, it yields directly decreased OER current during the activation process (Fig. S22). It is found that $LaNiO_3$ possesses the highest activation degree, and the substitution of Fe can inhibit this process with $LaFeO_3$ even showing a negative value (Fig. 2f). However, $LaNiO_3$ shows lower OER activity than $LaNi_{0.9}Fe_{0.1}O_3$. These results confirm the role of Fe substitution in controlling the activity and activation degree of $LaNiO_3$.

3.3 Surface Reconstruction Degree and Surface Reconstruction Rate Analysis

Compared with the crystalline as-obtained $LaNi_{0.9}Fe_{0.1}O_3$ (Fig. S23), a newly formed amorphous layer without long-range order is observed by high-resolution transmission electron microscopy (HRTEM) on the surface of reconstructed $LaNi_{0.9}Fe_{0.1}O_3$ (Fig. S24). This reconstruction process is shown in Fig. 3a. Without changing the crystal structure of the bulk phase as evidenced by XRD (Fig. S16), the depth for the outermost amorphous surface stays at 4.5 nm (Fig. S25). This thickness is demonstrated as optimal active surface depth for in-situ formed oxyhydroxides active species, which has been widely reported and accepted [50]. Meanwhile, we used EELS to investigate the reconstructed surface layer by obtaining an energy loss profile across the surface-bulk interface from Point 1 to Point 7 (Fig. S26a). Interestingly, compared with the profile obtained for the as-synthesized $LaNi_{0.9}Fe_{0.1}O_3$, the pre-edge feature at around 532 eV of the reconstructed $LaNi_{0.9}Fe_{0.1}O_3$ disappears at the surface region (Fig. S26b and c), suggesting an increase in oxygen vacancies on the surface. This evidence can further support the formation of amorphous surface layers after surface reconstruction. Fourier transform infrared (FTIR) spectra in Fig. S27 confirm the presence of MOOH structure by exhibiting a peak at ~ 1230 cm^{-1} after CV activation [51]. Thus, the element composition of this active surface layer is deduced as amorphous NiFe (oxy) hydroxide with abundant oxygen deficiencies. As shown in the XPS results, surface Ni and Fe cations exhibit higher oxidation states after activation (Fig. S28). The ICP-OES data further demonstrated that the overall Ni:Fe ratio shows no obvious change before (8:95:1.00) and after reconstruction (8:75:1.00). The kinetically stabilized Ni^{3+} due to Fe doping would induce a strong surface hydroxylation of the reconstructed $LaNi_{0.9}Fe_{0.1}O_3$ oxide and thus lead to the

formation of highly active $Ni_{0.9}Fe_{0.1}OOH$ to serve as the true reaction site for OER. For reconstructed $LaNi_{0.9}Fe_{0.1}O_3$ with active $Ni_{0.9}Fe_{0.1}OOH$ surface after 100 h CP measurement, the similar amorphous layer thickness of about 4.5 nm further indicates the stable structure of the reconstructed layer (Figs. S29 and S30). The short-range amorphization on the surface ensures the long-time stability of reconstructed $LaNi_{0.9}Fe_{0.1}O_3$ oxide because this amorphous layer might impede the proton transport into the bulk perovskite structure. In addition, DFT calculations demonstrate that the interface structure of $LaNi_{0.9}Fe_{0.1}O_3/Ni_{0.9}Fe_{0.1}OOH$ with lower binding energy (−80.32 eV) is much more stable than that of the $LaNiO_3/NiOOH$ (−79.59 eV), further keeping the reconstructed $LaNi_{0.9}Fe_{0.1}O_3$ an ideal durability (Fig. S31). Besides, it is worth noting that the thickness of newly formed reconstructed surface layers gradually decreases along with the increment of Fe content in the $LaNi_{1-x}Fe_xO_3$ series from 5.99 to 2.93 nm ($x = 0.00, 0.10, 0.25, 0.50, 0.75$) and even without obvious reconstruction layer for pure $LaFeO_3$ (Fig. 3b and c). Such a negative correlation demonstrates that Fe incorporation can suppress the surface reconstruction of $LaNi_{1-x}Fe_xO_3$ perovskite oxide. Moreover, the thickness (t) of the reconstructed surface layer or the reconstruction degree (t /1 nm) shows a similar trend consistent with the activation degree (Fig. 2f) of $LaNi_{1-x}Fe_xO_3$, while not consistent with their OER activity (Fig. 3d).

Potential-dependent in-situ Raman spectroscopy was further performed to monitor the dynamic surface reconstruction. In the obtained Raman spectra (Figs. 4a and S32a), the peaks at ~ 400 cm^{-1} are attributed to M–O bonds [52]. At this Raman shift, $LaNiO_3$ exhibits two peaks, while $LaNi_{0.9}Fe_{0.1}O_3$ shows only one. This is owing to their different inner structure induced by the incorporation of Fe, which results in different rates and degrees of surface reconstruction. The gradual emerging peaks at 460 and 550 cm^{-1} indicate the surface change from perovskite oxide to oxyhydroxide (MOOH) [52]. It should be noted that the peak of MOOH appears at 1.55 V for $LaNiO_3$ while such appearance occurred at 1.35 V for $LaNi_{0.9}Fe_{0.1}O_3$, indicating that Fe doping can accelerate the formation of oxyhydroxide layers. This is further illustrated by in-situ attenuated total reflection infrared (ATR-IR) spectra. As displayed in Figs. 4b and S32b, both the ATR-IR spectra of $LaNiO_3$ and $LaNi_{0.9}Fe_{0.1}O_3$ show two peaks from 900 to 4350 cm^{-1}. The peak at ~ 1200 cm^{-1} is associated with the O–O stretching mode
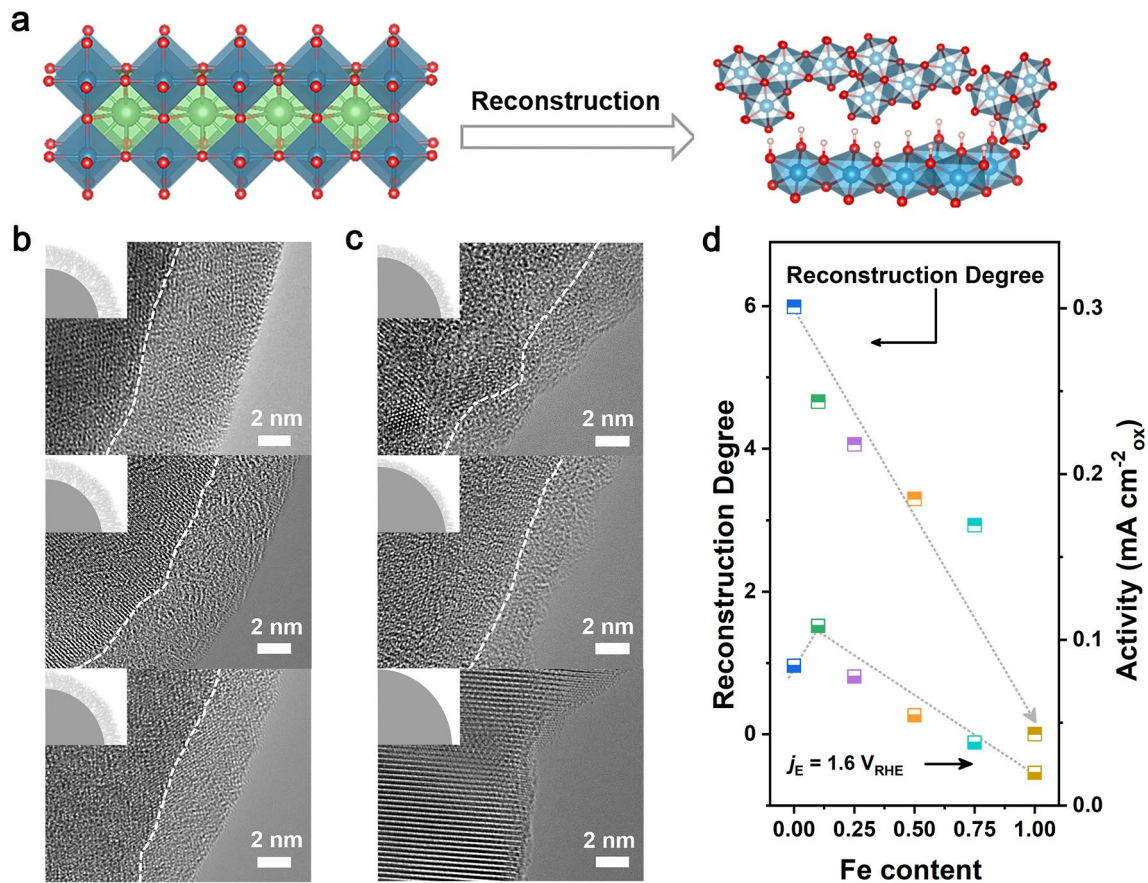
Fig. 3 **a** Schematic diagrams of the crystal structures before and after reconstruction. **b** The HRTEM images of the reconstructed $LaNiO_3$, $LaNi_{0.9}Fe_{0.1}O_3$, and $LaNi_{0.75}Fe_{0.25}O_3$ (from up to down). **c** HRTEM images of the reconstructed $LaNi_{0.5}Fe_{0.5}O_3$, $LaNi_{0.25}Fe_{0.75}O_3$, and $LaFeO_3$ (from up to down). **d** Current densities at 1.6 V and the thickness of the newly formed reconstructed surface layer for $LaNi_{1-x}Fe_xO_3$

of surface-adsorbed superoxide (OOH_{ads}), which is a typical reaction intermediate of AEM; while the adsorption band located at around 3400 cm^{-1} is attributed to surface-adsorbed OH species [53]. It is found that OH species appeared at a lower potential of 1.02 V for $LaNi_{0.9}Fe_{0.1}O_3$ compared with pure $LaNiO_3$ (1.22 V). This is consistent with the result from in-situ Raman spectra; that is, the incorporation of Fe can increase the reconstruction rate during the OER process. Besides, the emerged OOH_{ads} for $LaNi_{0.9}Fe_{0.1}O_3$ demonstrates that the lattice oxygen oxidation process (which corresponds to lattice oxygen mechanism, LOM) is suppressed after incorporating Fe compared to $LaNiO_3$. ^{18}O-labeled $LaNiO_3$ and $LaNi_{0.9}Fe_{0.1}O_3$ were analyzed by in-situ differential electrochemical mass spectroscopy (DEMS) to track the OER process in ^{16}O KOH electrolyte. It is noteworthy that compared with the $(^{36}O_2 + {}^{34}O_2)/{}^{32}O_2$ ratio of $LaNiO_3$ (34%), the ratio for

$LaNi_{0.9}Fe_{0.1}O_3$ is greatly decreased to 12% (Figs. 4c and d and S33). This obvious reduction indicates that the LOM process is greatly suppressed by Fe substitution, thus leading to a limited surface reassembly degree and enhanced structural stability. These results indicate that Fe ($x = 0.1$) doping accelerates the rate of surface reconstruction and promotes the formation of a stable surface structure prohibiting continuous reconstruction, thus leading to a reduced degree of reconstruction and enhanced structural stability.

3.4 Activation Degree, Reconstruction Degree, and Intrinsic Activity Analysis

In this study, we use the relative current change after surface reconstruction and the thickness of amorphous
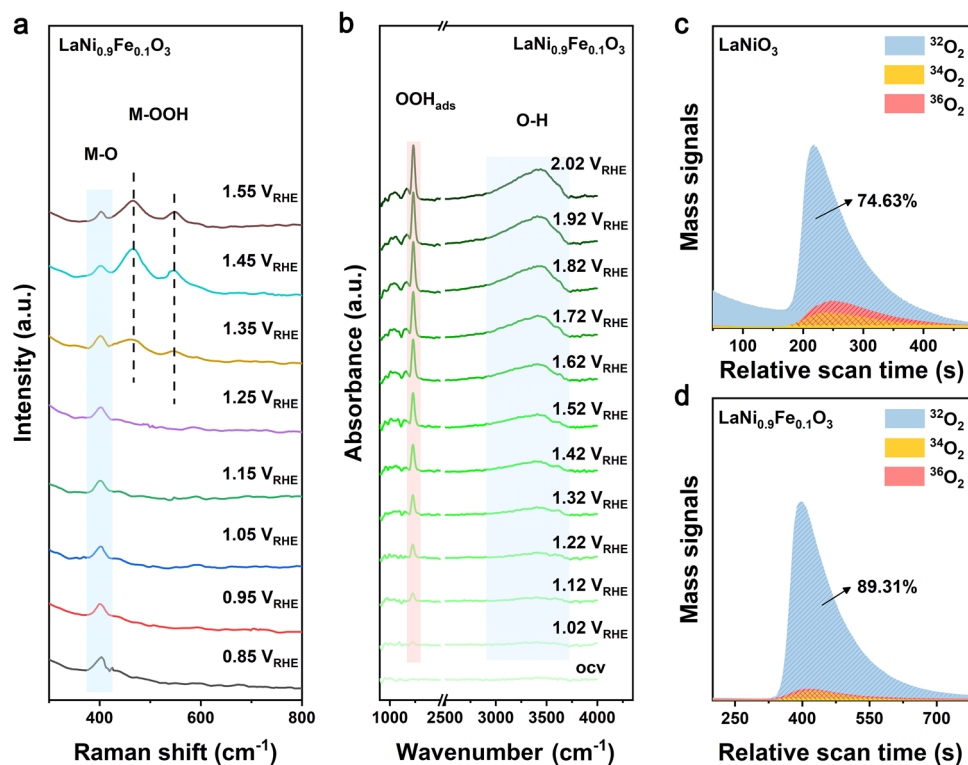
Fig. 4 **a** Potential-dependent in-situ Raman spectra of $LaNi_{0.9}Fe_{0.1}O_3$. **b** In-situ ATR-IR spectra recorded during the multi-potential steps for $LaNi_{0.9}Fe_{0.1}O_3$. **c** DEMS signals of $^{32}O_2$ ($^{16}O^{16}O$), and $^{34}O_2$ ($^{16}O^{18}O$) & $^{36}O_2$ ($^{18}O^{18}O$) from the reaction products for ^{18}O-labeled $LaNiO_3$. **d** DEMS signals of $^{32}O_2$ ($^{16}O^{16}O$), and $^{34}O_2$ ($^{16}O^{18}O$) & $^{36}O_2$ ($^{18}O^{18}O$) from the reaction products for.^{18}O-labeled $LaNi_{0.9}Fe_{0.1}O_3$

surface layers as measurable proxies for activation degree and reconstruction degree, respectively. To investigate the effect of electrochemical active surface formation, the relationship between activation degree, reconstruction degree (as defined in Methods), and OER activity of $LaNi_{1-x}Fe_xO_3$ are presented in Fig. 5. It is found that reconstruction degree is proportional to activation degree as both the reconstruction degree and activation degree gradually decrease along with the increment of Fe content in the $LaNi_{1-x}Fe_xO_3$ (Fig. 5a). This result demonstrates that the Fe doping can suppress the surface reconstruction and inhibit the activation degree of $LaNi_{1-x}Fe_xO_3$. However, as displayed in Fig. 5b and c, no meaningful correlation can be derived between OER activity and either the reconstruction degree or activation degree. Reconstructed $LaNiO_3$ with the maximum reconstruction degree and largest activation degree shows lower OER activity than reconstructed $LaNi_{0.9}Fe_{0.1}O_3$.

We thus believe that Fe doping can affect the OER activity of $LaNi_{1-x}Fe_xO_3$. Besides, different Ni/Fe ratio can also affect reconstruction degree and activation degree for $LaNi_{1-x}Fe_xO_3$. It has been widely accepted that the surface reconstruction of catalysts contributes largely to the outstanding OER activity, and thicker reconstructed surface layer results in more active sites of catalysts [54]. However, combined with our experimental results, we can deduce that the final OER activity is correlated with the bulk chemistry of the reconstructed surface and not the degree of surface rearrangement. Therefore, this observation calls for a more detailed study of the surface chemical properties of the pristine perovskite materials. In general, Fe ($x = 0.1$) doping can not only improve the reconstruction rate of $LaNiO_3$ but also decrease the activation degree and reconstruction degree with $LaNi_{0.9}Fe_{0.1}O_3/Ni_{0.9}Fe_{0.1}OOH$ showing the most stable interface structure for further catalysis.
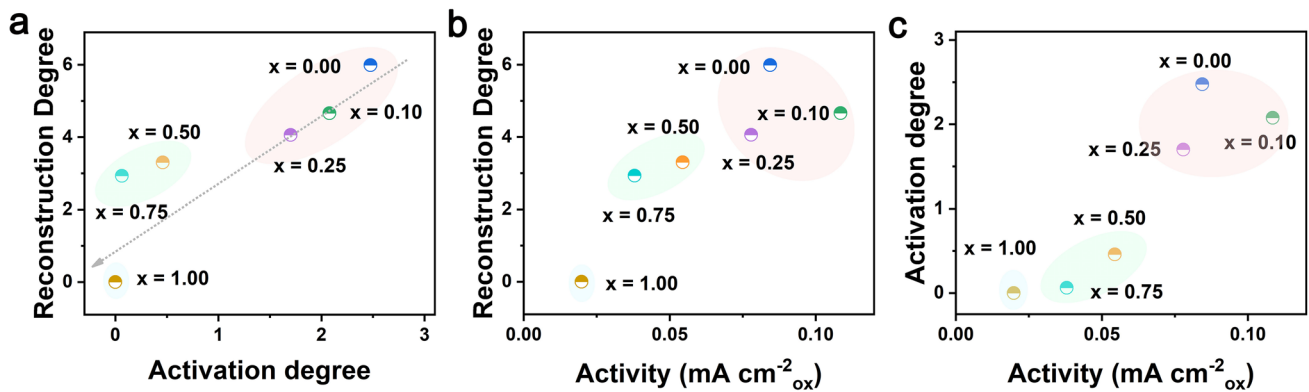
Fig. 5 **a** Relationship between activation degree and reconstruction degree. **b** Relationship between activity and reconstruction degree. **c** Relationship between activity and activation degree. The activation degree of LaFeO$_3$ is deemed as 0, because of its decreased OER current after surface reconstruction

As mentioned previously, Fe doping shows a direct effect on both OER activity and thickness of amorphous reconstructed surface layer. Hence, we performed DFT calculations to further investigate the mechanism of OER activity enhancement and surface reconstruction. The projected density of state (PDOS) of LaNiO$_3$, LaNi$_{0.9}$Fe$_{0.1}$O$_3$, and LaFeO$_3$ and their band center energies are presented in Fig. 6a. The incorporation of Fe into the perovskite is projected to shift the O 2p band center toward lower energy, farther away from the Fermi level (Fig. 6b). The PDOS results show that substitution of 10% Ni by Fe can reduce the O 2p level of LaNiO$_3$ from −1.811 to −1.882 eV. Earlier studies have revealed that uplifting the O 2p band level toward the Fermi level can result in a more dominant lattice oxygen oxidation mechanism for oxides. However, the oxidation of lattice oxygen is always featured with great surface reconstruction and thus inevitable structural instability [18]. Thus, due to the lowered O 2p band center, the lattice oxygen oxidation process is suppressed, resulting in enhanced structural stability of the surface of the Fe-doped perovskite. Moreover, the position of the O 2p band center shows a trend consistent with the activation degree (Fig. 2f) of LaNi$_{1-x}$Fe$_x$O$_3$, but inconsistent with their OER activity (Fig. 6c). We thus believe that the OER activity of LaNi$_{1-x}$Fe$_x$O$_3$ oxides is dominated by the surface structure and composition after self-rearrangement, while their surface reconstruction degree is governed by the predicted O 2p level.

4 Conclusions

In summary, with LaNi$_{1-x}$Fe$_x$O$_3$ perovskite oxides as research model, we found that Fe substitution can manipulate the intrinsic activity, activation degree, reconstruction degree, and reconstruction rate. Among these substituted oxides, LaNi$_{0.9}$Fe$_{0.1}$O$_3$ after surface reconstruction exhibits the best electrocatalytic performance. The volcano-shaped activity trend and the thinning of reconstructed surface with the increase of Fe doping demonstrate that OER activity mainly depends on the composition of the LaNi$_{1-x}$Fe$_x$O$_3$ perovskite, while not the surface reconstruction degree. The reconstructed amorphous layer composed of highly active Ni$_{0.9}$Fe$_{0.1}$OOH on LaNi$_{0.9}$Fe$_{0.1}$O$_3$ with balanced reconstruction degree and reconstruction rate shows outstanding intrinsic catalytic activity and long-term stability. By combining experimental measurements and theoretical calculations, we found that Fe substitution in LaNiO$_3$ perovskite oxide can facilitate Ni^{3+} to reach dynamic equilibrium, leading to a stable active reconstructed layer. The downshift of O 2p band center by Fe incorporation suppresses the oxidation of lattice oxygen under OER conditions and thus provides stable surface chemistry to contribute excellent stability. The findings here illustrate the importance of surface composition after reconstruction, which is more significant in determining the activity than the degree of surface reconstruction.
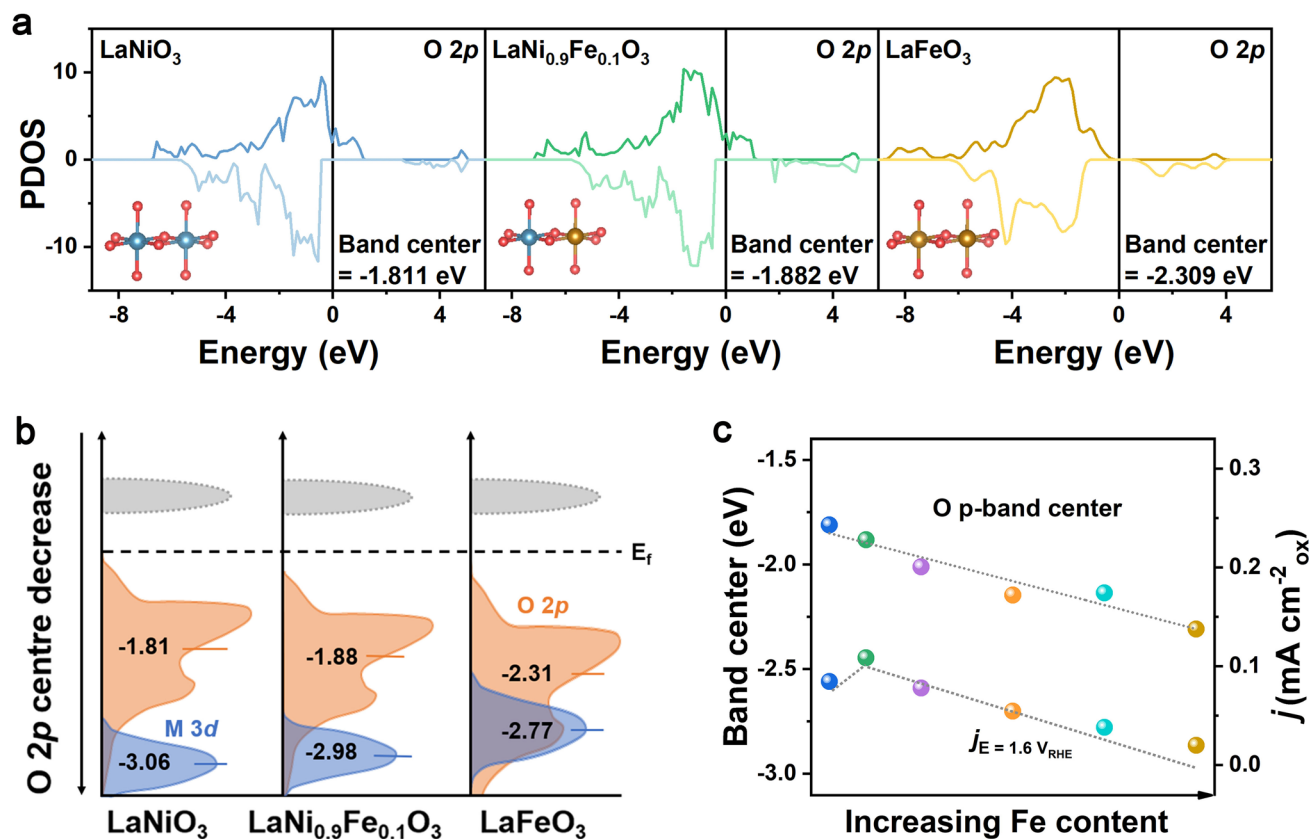
Fig. 6 **a** Computed M 3*d* and O 2*p* PDOS of $LaNiO_3$, $LaNi_{0.9}Fe_{0.1}O_3$, and $LaNi_{0.75}Fe_{0.25}O_3$. **b** Schematic band diagrams of $LaNiO_3$, $LaNi_{0.9}Fe_{0.1}O_3$ and $LaFeO_3$. **c** Current densities at 1.6 V and the O 2*p* band center relative to the Fermi level for $LaNi_{1-x}Fe_xO_3$

Declarations

References

1. A. Li, S. Kong, K. Adachi, H. Ooka, K. Fushimi et al., Atomically dispersed hexavalent iridium oxide from MnO_2 reduction for oxygen evolution catalysis. Science **384**, 666 (2024). https://doi.org/10.1126/science.adg5193

2. M. Liu, J. Zhang, H. Su, Y. Jiang, W. Jiang et al., In situ modulating coordination fields of single-atom cobalt catalyst for enhanced oxygen reduction reaction. Nat. Commun. **15**, 1675 (2024). https://doi.org/10.1038/s41467-024-45990-w

3. Z. Zhang, C. Jia, P. Ma, C. Feng, J. Yang et al., Distance effect of single atoms on stability of cobalt oxide catalysts for acidic oxygen evolution. Nat. Commun. **15**, 1767 (2024). https://doi.org/10.1038/s41467-024-46176-0

4. Z. Weng, L. Guo, Y. Wei, L. Liu, P. Xi et al., Progress of synthesis of rare-earth perovskite oxides and their application in energy conversion and storage. J. Chin. Rare Earth Soc. (2021). https://doi.org/10.11785/S1000-4343.20210101

5. T. Wu, X. Ren, Y. Sun, S. Sun, G. Xian et al., Spin pinning effect to reconstructed oxyhydroxide layer on ferromagnetic oxides for enhanced water oxidation. Nat. Commun. **12**, 3634 (2021). https://doi.org/10.1038/s41467-021-23896-1

6. X. Ren, T. Wu, Y. Sun, Y. Li, G. X, et al., Spin-polarized oxygen evolution reaction under magnetic field. Nat. Commun. **12**, 2608 (2021). https://doi.org/10.1038/s41467-021-22865-y

7. J. Chang, Y. Shi, H. Wu, J. Yu, W. Jing et al., Oxygen radical coupling on short-range ordered Ru atom arrays enables exceptional activity and stability for acidic water oxidation. J. Am. Chem. Soc. **146**, 12958 (2024). https://doi.org/10.1021/jacs.3c13248

8. A. Fungerlings, M. Wohlgemuth, D. Antipin, E. Var der Mine, E. Kiens et al., Crystal-facet-dependent surface transformation dictates the oxygen evolution reaction activity in lanthanum nickelate. Nat. Commun. **14**, 8284 (2023). https://doi.org/10.1038/s41467-023-43901-z

9. S. Tiwari, J. Koenig, G. Poillerat, R. Singh, Electrocatalysis of oxygen evolution/reductionon $LaNiO_3$ prepared by a novel malic acid-aided method. J. Appl. Electrochem. **28**, 114 (1998). https://doi.org/10.1023/A:1003214321780

10. C. Baeumer, J. Li, Q. Lu, Y.-L. Liang, L. Jin et al., Tuning electrochemically driven surface transformation in atomically flat $LaNiO_3$ thin films for enhanced water electrolysis. Nat. Mater. **20**, 674 (2021). https://doi.org/10.1038/s41563-020-00877-1

11. J. Petrie, V. Cooper, J. Freeland, T. Meyer, Z. Zhang et al., Enhanced bifunctional oxygen catalysis in strained $LaNiO_3$ perovskites. J. Am. Chem. Soc. **138**, 2488 (2016). https://doi.org/10.1021/jacs.5b11713

12. J. Liu, E. Jia, K.A. Stoerzinger, L. Wang, Y. Wang et al., Dynamic lattice oxygen participation on perovskite $LaNiO_3$ during oxygen evolution reaction. J. Phys. Chem. C **124**, 15386 (2022). https://doi.org/10.1021/acs.jpcc.0c04808

13. L. Magnier, G. Cossard, V. Martin, C. Pascal, V. Roche et al., Fe–Ni-based alloys as highly active and low-cost oxygen evolution reaction catalyst in alkaline media. Nat. Mater. **23**, 252 (2024). https://doi.org/10.1038/s41563-023-01744-5

14. Y.-H. Wu, M. Janák, P.M. Abdala, C.N. Borca, A. Wach et al., Probing surface transformations of lanthanum nickelate electrocatalysts during oxygen evolution reaction. J. Am. Chem. Soc. **146**, 11887 (2024). https://doi.org/10.1021/jacs.4c00863

15. M. Stevens, C. Trang, L. Enman, J. Deng, S. Boettcher, Reactive Fe-sites in Ni/Fe (oxy)hydroxide are responsible for exceptional oxygen electrocatalysis activity. J. Am. Chem. Soc. **139**, 11361 (2019). https://doi.org/10.1021/jacs.7b07117

16. L. Trotochaud, S.L. Young, J.K. Ranney, S.W. Boettcher, Nickel-iron oxyhydroxide oxygen-evolution electrocatalysts: the role of intentional and incidental iron incorporation. J. Am. Chem. Soc. **136**, 6744 (2014). https://doi.org/10.1021/ja502379c

17. C. Kuai, C. Xi, A. Hu, Y. Zhang, Z.J. Xu et al., Revealing the dynamics and roles of iron incorporation in nickel hydroxide water oxidation catalysts. J. Am. Chem. Soc. **143**, 18519 (2021). https://doi.org/10.1021/jacs.1c07975

18. T. Wu, S. Sun, J. Song, S. Xi, Y. Du, Iron-facilitated dynamic active-site generation on spinel $CoAl_2O_4$ with self-termination of surface reconstruction for water oxidation. Nat. Catal. **2**, 763 (2019). https://doi.org/10.1038/s41929-019-0325-4

19. W. Wan, Y. Zhao, S. Wei, C. Triana, J. Li et al., Mechanistic insight into the active centers of single/dual-atom Ni/Fe-based oxygen electrocatalysts. Nat. Commun. **12**, 5589 (2021). https://doi.org/10.1038/s41467-021-25811-0

20. Y. Sun, S. Sun, H. Yang, S. Xi, J. Gracia et al., Spin-related electron transfer and orbital interactions in oxygen electrocatalysis. Adv. Mater. **32**, 2003297 (2020). https://doi.org/10.1002/adma.202003297

21. H. Li, Y. Chen, J. Liu, A. Fisher, J. Ager et al., Surface reconstruction of perovskites for water oxidation: the role of initial oxides' bulk chemistry. Small Sci. **2**, 2100048 (2021). https://doi.org/10.1002/smsc.202100048

22. Y. Duan, S. Sen, S. Xi, X. Ren, Y. Zhou, Tailoring the Co 3d-O 2p covalency in $LaCoO_3$ by Fe substitution to promote oxygen evolution reaction. Chem. Mater. **29**, 10534 (2017). https://doi.org/10.1021/acs.chemmater.7b04534

23. H. Wang, J. Wang, Y. Pi, Q. Shao, Y. Tan et al., Double perovskite $LaFe_xNi_{1-x}O_3$ nanorods enable efficient oxygen evolution electrocatalysis. Angew. Chem. Int. Ed. **58**, 2316 (2019). https://doi.org/10.1002/anie.201812545

24. X. Liang, L. Shi, Y. Liu, H. Chen, R. Si et al., Activating inert, nonprecious perovskites with iridium dopants for efficient oxygen evolution reaction under acidic conditions. Angew. Chem. Int. Ed. **58**, 7631 (2022). https://doi.org/10.1002/anie.201900796

25. Y. Zhou, S. Sun, J. Song, S. Xi, B. Chen et al., Enlarged Co–O covalency in octahedral sites leading to highly efficient spinel oxides for oxygen evolution reaction. Adv.

Mater. **30**, 1802912 (2018). https://doi.org/10.1002/adma.201802912

26. G. Chen, Y. Zhu, H. Ming, Z. Hu, S.-F. Hung et al., An amorphous nickel–iron-based electrocatalyst with unusual local structures for ultrafast oxygen evolution reaction. Adv. Mater. **31**, 1900883 (2019). https://doi.org/10.1002/adma.201900883

27. H. Wang, J. Qi, N. Yang, W. Cui, J. Wang et al., Dual-defects adjusted crystal-field splitting of $LaCo_{1-x}Ni_xO_{3-\delta}$ hollow multi-shelled structures for efficient oxygen evolution. Angew. Chem. Int. Ed. **59**, 1969 (2020). https://doi.org/10.1002/anie.202007077

28. C. Hu, X. Wang, T. Yao, T. Gao, J. Han et al., Enhanced electrocatalytic oxygen evolution activity by tuning both the oxygen vacancy and orbital occupancy of B-site metal cation in $NdNiO_3$. Adv. Funct. Mater. **29**, 1902449 (2019). https://doi.org/10.1002/adfm.201902449

29. L. Wang, P. Adiga, J. Zhao, W.S. Samarakoon, K.A. Stoerzinger et al., Understanding the electronic structure evolution of epitaxial $LaNi_{1-x}Fe_xO_3$ thin films for water oxidation. Nano Lett. **21**, 8324 (2021). https://doi.org/10.1021/acs.nanolett.1c02901

30. X. Wang, Z. Pan, X. Chu, K. Huang, Y. Cong et al., Atomic-scale insights into surface lattice oxygen activation at the spinel/perovskite interface of $Co_3O_4/La_{0.3}Sr_{0.7}CoO_3$. Angew. Chem. Int. Ed. **58**, 11720 (2019). https://doi.org/10.1002/anie.201905543

31. J. Huang, H. Sheng, R.D. Ross, J. Han, X. Wang et al., Modifying redox properties and local bonding of Co_3O_4 by CeO_2 enhances oxygen evolution catalysis in acid. Nat. Commun. **12**, 3036 (2021). https://doi.org/10.1038/s41467-021-23390-8

32. Z.-F. Huang, J. Song, Y. Du, S. Xi, S. Dou et al., Chemical and structural origin of lattice oxygen oxidation in Co–Zn oxyhydroxide oxygen evolution electrocatalysts. Nat. Energy **4**, 329 (2019). https://doi.org/10.1038/s41560-019-0355-9

33. Y. Wei, Y. Hu, P. Da, Z. Weng, P. Xi et al., Triggered lattice-oxygen oxidation with active-site generation and self-termination of surface reconstruction during water oxidation. Proc. Natl. Acad. Sci. U.S.A. (2023). https://doi.org/10.1073/pnas.23122241

34. T.E. Westre, P. Kenepohl, J.G. Dewitt, B. Hedman, K.O. Hodgson et al., A multiplet analysis of Fe K-edge 1s → 3d pre-edge features of iron complexes. J. Am. Chem. Soc. **119**, 6297 (1997). https://doi.org/10.1021/ja964352a

35. J. Wang, S.-J. Kim, J. Liu, Y. Gao, S. Choi et al., Redirecting dynamic surface restructuring of a layered transition metal oxide catalyst for superior water oxidation. Nat. Catal. **4**, 212 (2021). https://doi.org/10.1038/s41929-021-00578-1

36. S. Zhou, X. Miao, X. Zhao, C. Ma, Y. Qiu et al., Engineering electrocatalytic activity in nanosized perovskite cobaltite through surface spin-state transition. Nat. Commun. **7**, 11510 (2016). https://doi.org/10.1038/ncomms11510

37. P.P. Lopes, D.Y. Chung, X. Rui, H. Zheng, H. He et al., Dynamically stable active sites from surface evolution of perovskite materials during the oxygen evolution reaction. J. Am. Chem. Soc. **143**, 2741 (2021). https://doi.org/10.1021/jacs.0c08959

38. X. Ren, C. Wei, Y. Sun, X. Liu, F. Meng et al., Constructing an adaptive heterojunction as a highly active catalyst for the oxygen evolution reaction. Adv. Mater. **32**, 2001292 (2020). https://doi.org/10.1002/adma.202001292

39. C. Kuai, Z. Xu, C. Xi, A. Hu, Z. Yang et al., Phase segregation reversibility in mixed-metal hydroxide water oxidation catalysts. Nat. Catal. **3**, 743 (2020). https://doi.org/10.1038/s41929-020-0496-z

40. J. Scachez, M. Stevens, A. Young, A. Gallo, M. Zhao et al., Isolating the electrocatalytic activity of a confined NiFe motif within zirconium phosphate. Adv. Energy Mater. **11**, 2003545 (2021). https://doi.org/10.1002/aenm.202003545

41. Y. Lee, J. Suntivich, K. May, E. Perry, S.-H. Yang, Synthesis and activities of rutile IrO_2 and RuO_2 nanoparticles for oxygen evolution in acid and alkaline solutions. J. Phys. Chem. Lett. **3**, 399 (2012). https://doi.org/10.1021/jz2016507

42. G. Chen, Z. Hu, Y. Zhu, B. Gu, Y. Zhong et al., A universal strategy to design superior water-splitting electrocatalysts based on fast in situ reconstruction of amorphous nanofilm precursors. Adv. Mater. **30**, 1804333 (2018). https://doi.org/10.1002/adma.201804333

43. P. Chakthranont, J. Kibsgaard, A. Gallo, J. Park, M. Mitani et al., Effects of gold Substrates on the intrinsic and extrinsic activity of high-loading nickel-based oxyhydroxide oxygen evolution catalysts. ACS Catal. **7**, 5399 (2017). https://doi.org/10.1021/acscatal.7b01070

44. F. Song, X. Hu, Exfoliation of layered double hydroxides for enhanced oxygen evolution catalysis. Nat. Commun. **5**, 4477 (2014). https://doi.org/10.1038/ncomms5477

45. Y. Duan, S. Sun, Y. Sun, S. Xi, X. Chi et al., Mastering surface reconstruction of metastable spinel oxides for better water oxidation. Adv. Mater. **31**, 1807898 (2019). https://doi.org/10.1002/adma.201807898

46. F. Dionigi, Z. Zeng, L. Sinev, T. Merzdorf, S. Deshpande et al., In-situ structure and catalytic mechanism of NiFe and CoFe layered double hydroxides during oxygen evolution. Nat. Commun. **11**, 2522 (2020). https://doi.org/10.1038/s41467-020-16237-1

47. Y. Wang, L. Yan, K. Dastafkan, C. Zhao, X. Zhao et al., Lattice matching growth of conductive hierarchical porous MOF/LDH heteronanotube arrays for highly efficient water oxidation. Adv. Mater. (2021). https://doi.org/10.1002/adma.202006351

48. M. Chen, N. Kitiphatpiboon, C. Feng, A. Abudula, Y. Ma et al., Recent progress in transition-metal-oxide-based electrocatalysts for the oxygen evolution reaction in natural seawater splitting: a critical review. eScience **3**, 100111 (2023). https://doi.org/10.1016/j.esci.2023.100111

49. A.S. Kelsey, R. Marcel, H.B. Hong, S.-H. Yang, Orientation-dependent oxygen evolution activities of rutile IrO_2 and RuO_2. J. Phys. Chem. Lett. **5**, 1636 (2014). https://doi.org/10.1021/jz500610u

50. S. Lee, A. Moysiadou, Y.-C. Chu, H. Chen, X. Hu, Tracking high-valent surface iron species in the oxygen evolution reaction on cobalt iron (oxy)hydroxide. Energy Environ. Sci. **15**, 206 (2021). https://doi.org/10.1039/D1EE02999A

51. Q. Ji, Y. Kong, C. Wang, H. Tan, H. Duan et al., Lattice strain induced by linker scission in metal–organic framework nanosheets for oxygen evolution reaction. ACS Catal. **10**, 5691 (2020). https://doi.org/10.1021/acscatal.0c00989

52. M. Louie, T. Alexis, An investigation of thin-film Ni–Fe oxide catalysts for the electrochemical evolution of oxygen. J. Am. Chem. Soc. **135**, 12329 (2013). https://doi.org/10.1021/ja405351s

53. N. Zhang, Y. Hu, L. An, Q.Y. Li, J. Yin et al., Surface activation and Ni–S stabilization in NiO/NiS_2 for efficient oxygen evolution reaction. Angew. Chem. Int. Ed. (2022). https://doi.org/10.1002/anie.202207217

54. Y. Yao, S. Hu, W. Chen, Z.-Q. Huang, W. Wei, Engineering the electronic structure of single atom Ru sites via compressive strain boosts acidic water oxidation electrocatalysis. Nat. Catal. **2**, 304 (2019). https://doi.org/10.1038/s41929-019-0246-2

55. G. Kresse, J. Furthmuller, Efficient iterative schemes for ab initio total-energy calculations using a plane-wave basis set. Phys. Rev. B **54**, 11169 (1996). https://doi.org/10.1103/PhysRevB.54.11169

56. J. Perdew, K. Burke, M. Ernzerhof, Generalized gradient approximation made simple. Phys. Rev. B **54**, 11169 (1996). https://doi.org/10.1103/PhysRevLett.77.3865

57. S. Grimme, J. Antony, S. Ehrlich, H. Krieg, A consistent and accurate ab initio parametrization of density functional dispersion correction (DFT-D) for the 94 elements H-Pu. J. Chem. Phys. **132**, 154104 (2010). https://doi.org/10.1063/1.3382344

58. N. Shuichi, Constant temperature molecular dynamics methods. Prog. Theory Phys. Supp. **103**, 1 (1991). https://doi.org/10.1143/PTPS.103.1

Publisher's Note Springer Nature remains neutral with regard to jurisdictional claims in published maps and institutional affiliations.